

Numerical simulation of magnetized jet creation using a hollow ring of laser beams

Cite as: Phys. Plasmas **26**, 022902 (2019); doi: [10.1063/1.5050924](https://doi.org/10.1063/1.5050924)

Submitted: 3 August 2018 · Accepted: 15 January 2019 ·

Published Online: 4 February 2019



View Online



Export Citation



CrossMark

Y. Lu,^{1,2} P. Tzeferacos,³ E. Liang,¹ R. K. Follett,⁴ L. Gao,⁵ A. Birkel,⁶ D. H. Froula,⁴ W. Fu,¹ H. Ji,⁵ D. Lamb,³ C. K. Li,⁶ H. Sio,⁶ R. Petrasso,⁶ and M. S. Wei⁴

AFFILIATIONS

¹Department of Physics and Astronomy, Rice University, Houston, Texas 77005, USA

²Theoretical Division, Los Alamos National Laboratory, Los Alamos, New Mexico 87545, USA

³Department of Astronomy and Astrophysics, University of Chicago, Chicago, Illinois 60637, USA

⁴Laboratory for Laser Energetics, University of Rochester, Rochester, New York 14623, USA

⁵Princeton Plasma Physics Laboratory, Princeton, New Jersey 08540, USA

⁶Plasma Science and Fusion Center, Massachusetts Institute of Technology, Cambridge, Massachusetts 02139, USA

ABSTRACT

Three dimensional FLASH magneto-hydrodynamic modeling is carried out to interpret the OMEGA laser experiments of strongly magnetized, highly collimated jets driven by a ring of 20 OMEGA beams. The predicted optical Thomson scattering spectra and proton images are in good agreement with a subset of the experimental data. Magnetic fields generated via the Biermann battery term are amplified at the boundary between the core and the surrounding of the jet. The simulation predicts multiple axially aligned magnetic flux ropes with an alternating poloidal component. Future applications of the hollow ring configuration in laboratory astrophysics are discussed.

Published under license by AIP Publishing. <https://doi.org/10.1063/1.5050924>

I. INTRODUCTION

Supersonic, well collimated outflows are ubiquitous in many astrophysical systems, such as young stellar objects (YSOs),¹ active galactic nuclei (AGN),² and gamma-ray bursts (GRBs).³ Despite various astronomical observations, theoretical studies, and numerical modelings of astrophysical jets, many fundamental questions remain, e.g., launching mechanism, composition, and morphology of the magnetic field and stability. Magnetic fields permeate the universe, but their origin is not fully understood, especially in astrophysical jets. A variety of ideas have been proposed in which seed magnetic fields could be created. However, this mechanism has only been demonstrated in the laboratory recently.^{4,5}

With advances in large laser facilities, scalable laboratory experiments to study astrophysical phenomena have become achievable. Over the years, experiments have been performed to study astrophysics utilizing high-intensity lasers at the OMEGA laser facility at the Laboratory for Laser Energetics (LLE), the National Ignition Facility (NIF) at Lawrence Livermore National Laboratory, and laser facilities in other countries.^{6–13} Laboratory produced jets with proper dimensionless parameters may

provide an alternative platform to study the jets of astrophysical scales.

A new way of launching high density and high temperature plasma jets using multiple intense laser beams is to utilize the hollow ring configuration as proposed by Fu *et al.*^{14,15} It was demonstrated in two dimensional numerical simulations that a bundle of laser beams of given individual intensity, duration, and focal spot size produces a supersonic jet of higher density, temperature, and better collimation if the beams are focused to form a circular ring pattern on a flat target instead of a single focal spot. The Biermann Battery ($\nabla n_e \times \nabla T_e$) term¹⁶ can generate and sustain strong toroidal fields downstream in the collimated jet outflow far from the target surface. Those simulations were carried out in two dimensional cylindrical geometry, where the intensity variation along the ring due to individual laser beams was neglected. Three dimensional simulations are necessary to understand the formation and evolution of the jet in the actual experiments.

The ring jet experiments were designed and carried out on the OMEGA laser facility¹⁷ in 2015 and 2016.¹⁸ We used 20 OMEGA beams to simultaneously irradiate the target forming a

ring pattern. Each beam delivers 500 J of energy in 1 ns. In this paper, we aim to use three dimensional FLASH¹⁹ simulations to explain the observed jet parameters in the experiments. Using the magneto-hydrodynamic (MHD) results, we can predict the diagnostic outcomes from first principles. In Sec. II, we describe the experimental design to produce laboratory jets on the OMEGA laser and the simulation methods to model the experiment. Simulation results are discussed in Sec. III. The validation against a subset of experimental data is discussed in Sec. IV.

II. SIMULATION METHODS

A. Non-ideal magneto-hydrodynamics in the FLASH code

The FLASH code²⁰ is used to carry out the detailed physics simulations of our laser experiments to study the formation and dynamics of the jet and the origin of magnetic fields. FLASH^{19,21} is a publicly available, multi-physics, highly scalable parallel, finite-volume Eulerian code and framework whose capabilities include adaptive mesh refinement (AMR), multiple hydrodynamic and MHD solvers, and implicit solvers for diffusion using the HYPRE library and laser energy deposition. FLASH is capable of using multi-temperature equation of states and multi-group opacities. Magnetic field generation via the Biermann battery term has been implemented and studied in FLASH recently.²²

We use the same FLASH code units as in Ref. 4 to solve the three-temperature non-ideal MHD equations. A cartesian grid with (256 × 256 × 512) zones is used to resolve a (3 mm × 3 mm × 6 mm) domain, corresponding to ~11 μm per cell width. The number of cells we use is sufficient to resolve the spatial distribution of all the quantities that the plasma diagnostics are able to resolve in the OMEGA experiments. We did test runs at different resolutions and the simulation converged at a cell width of 11 μm. The plasma has zero initial magnetic field. The laser target is modeled as a 3 mm diameter and 0.5 mm thick disk with the composition listed in Table I. To model the material properties of the CH and CH+dopant targets, we utilize the opacity and EoS tables computed with PROPACEOS.²³ We use the equation of state of helium in the chamber with an initial density equal to 2 × 10⁻⁷ g/cc, which should have been vacuum. The helium does not affect the simulation significantly, as the mass, momentum, and energy budget in the modeled helium is much less than 1%. To suppress the magnetic field from the numerical artefact, we turn off the Biermann battery term and use the largest allowed magnetic resistivity in the explicit solver for each time step in the regions with a density lower than 2 × 10⁻⁵ g/cm³. The electron heat conduction is calculated using the Braginskii model²⁴ in a weak magnetic field limit.

To model the laser driven blowoffs, we use the spatial and temporal specifications of each of the twenty OMEGA driver beams. The 20 driver beams are turned on and turned off

TABLE I. Target characteristics used in the experiments and the simulations.

Composition (number fraction)	Density	Laser target ring radius
C(50%) H(50%)	1.04 g/cc	0, 400, 800, 1200 μm
C(49%) H(49%) Fe(2%)	1.21 g/cc	800, 1200 μm

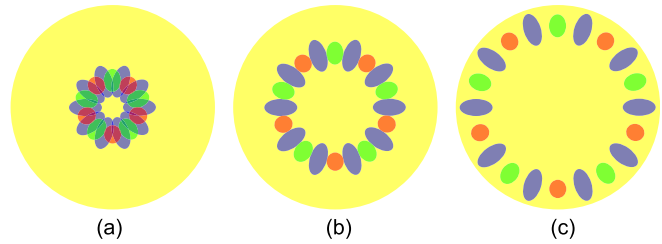


FIG. 1. The illuminated area on the target by 20 OMEGA beams. The transverse sections of the beams are circles, but the spots on the target surface are ellipses due to inclination. The incident angle is 59° for the blue spot, 42° for the green spot, and 21° for the red spot. (a) d = 400 μm ring radius; (b) d = 800 μm ring radius; (c) d = 1200 μm ring radius. The d = 0 case is not shown. Note that the red and green spots form a 5-fold symmetry, and the blue spots form a 10-fold symmetry.

simultaneously with a 1 ns pulse duration. Each delivers 500 J of energy on a target flat-top. The radius of each beam is 125 μm. The laser spots are arranged to form a ring pattern of radius d, as shown in Fig. 1. The target is 0.5 mm thick to prevent the burn-through. The setup of the diagnostics is sketched in Fig. 2 and discussed in Secs. II B and II C.

For convention, t = 0 is the time for laser turn on. The z direction is perpendicular to the surface of the target plane. The jet is formed in the z > 0 region. We also use cylindrical coordinates, where r = 0 is the central axis of the target. The target surface is located at z = 0. The axial direction is along the z axis. The toroidal or azimuthal direction is the φ direction in the cylindrical coordinate system. The target chamber center (TCC) is at x = y = r = 0, z = 0.25 cm.

B. Optical Thomson scattering

Optical Thomson scattering^{25,26} is used to probe the electron/ion temperatures, electron density, and flow velocity at TCC. We used one probe beam with a pulse of 1 ns, an energy of

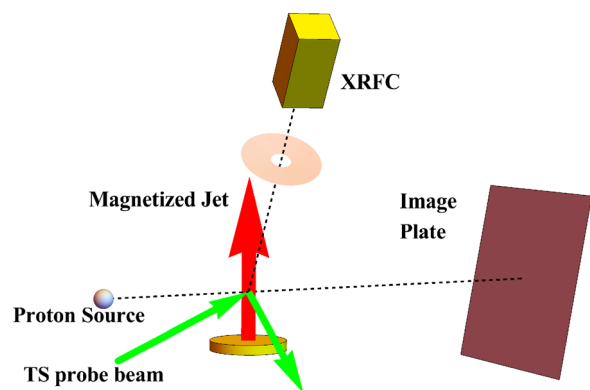


FIG. 2. Schematics of the diagnostics setup of OMEGA magnetized jet experiments. For DD and D³He protons, the source stands 1 cm from TCC, while the image plate CR39 is located 17 cm from TCC on the other side. For the TNSA protons, the source stands 0.8 cm from TCC, while the radiochromic film pack is located 16.5 cm from TCC on the other side. The X-ray framing camera (XRFC) images the jet at 38° from the axis, which is not modeled in this work.

25–50 J, and a wavelength (2ω) of 532 nm as the backlighter. The intensity distribution of the probe beam is $70\ \mu\text{m}$ FWHM 2D Gaussian.

We model the Thomson scattering spectrum using the 3D FLASH simulation results. The spatial profiles of electron density, electron/ion temperature, flow velocity, and mass fraction of species are taken as the input for the spectroscopy code.²⁷ The heating by the probe beam is modeled by laser absorption. The dispersion relations for the ion acoustic wave and the electron plasma wave²⁷ are used to calculate the power output. The final power output is weight averaged by the spatial intensity distribution of the probe laser. The instrument broadening²⁸ is taken into account in the modeling spectrum.

The experimental data are also fitted using the model (see more results in Ref. 18) to compare with the plasma quantities averaged $(200\ \mu\text{m})^3$ cube centered at TCC.

C. Proton radiography

Our OMEGA experiments used two types of proton sources to map out the magnetic fields (1) DD (3 MeV) and D^3He (14.7 MeV) protons from fusion reaction driven by 24 OMEGA beams.^{29,30} The actual spectrum is typically an up-shifted symmetric Gaussian distribution, FWHM = 320 keV centered at 3.6 MeV for DD protons and FWHM = 670 keV centered at 15.3 MeV for D^3He protons. The emitting position of protons follows a 3D Gaussian distribution with an e-fold radius equal to $20\ \mu\text{m}$, and the burn time is 150 ps;³⁰ (2) Broadband protons up to 60 MeV are driven by an OMEGA EP beam via the Target Normal Sheath Acceleration (TNSA) mechanism.³¹ The actual spectrum is typically an exponential distribution with an effective temperature of 3.79 MeV for our copper backlighter target.³² The initial position of protons at the source follows a 3D Gaussian distribution with an e-fold radius equal to $5\ \mu\text{m}$,³⁰ and the pulse duration is 1 ps. For the DD and D^3He protons, the source stands 1 cm from TCC, while the image plate CR39 is located 17 cm from TCC on the other side. For the TNSA protons, the source stands 0.8 cm from TCC, while the radiochromic film pack is located 16.5 cm from TCC on the other side.

The modeling for proton radiography is composed of (1) sampling for the source distributions mentioned above, (2) solving the trajectory of the protons, and (3) recording the protons on the detector plane.

The deflection of protons in electromagnetic fields is calculated by solving the Newton-Lorentz equation

$$\frac{d(m_p v)}{dt} = e \left(\mathbf{E} + \frac{\mathbf{v}}{c} \times \mathbf{B} \right). \quad (1)$$

In a typical MHD fluid, $E \approx \frac{v_h}{c} B$, where v_h is the hydrodynamical velocity scale of the fluid. The ratio of electric force to magnetic force is $\frac{E}{(v_p/c)B} \approx \frac{v_h}{v_p}$. For a proton with energy larger than $\sim\text{MeV}$, the proton speed v_p is much larger than v_h , so we use electric field $\mathbf{E} = 0$ approximation in the modeling. The energy lost is calculated throughout the proton motion from the NIST PSTAR table.³³ Protons lose a significant amount of energy in the remaining solid target with the density of $\sim 1\ \text{g/cc}$.

We assume that the detector for DD protons has uniform sensitivity for protons with $E > 2\ \text{MeV}$ and that for D^3He protons has uniform sensitivity for all protons with $E > 14.4\ \text{MeV}$. The TNSA proton energy range that each film is primarily sensitive to is $E > E_0$, and the deposited energy per proton is proportional to $(E - E_0)^{-1/2}$, while no energy is deposited for $E < E_0$. The characteristic energy E_0 is different for each pack in the radiochromic film. Temporal smearing of TNSA proton images is neglected because the pulse duration is short. Temporal smearing of DD and D^3He protons is calculated using the integral of the second order interpolation among successive images with 0.1 ns intervals.

III. FLASH SIMULATION RESULTS

A. Hydrodynamics

The jet is formed by the merging of the plasma plumes produced by 20 individual OMEGA beams through a strong cylindrical shock. By using a large ring radius, the flows will not collide immediately while the lasers irradiate the target. For the collision at later time with more available room, the flows develop larger radial velocities which become more supersonic. Thus, a stronger cylindrical shock is generated near the z axis. For the cylindrical shock, the surrounding is in the upstream region, and the central core is in the downstream region. It is a hydrodynamic shock where the plasma β is much larger than unity. Figure 3 shows the time evolution of the jet for $d = 800\ \mu\text{m}$ CH target simulation. The jet is supersonic and well collimated. The jets with different ring radii all travel several millimeters by $t = 3\ \text{ns}$. The jet keeps traveling and expanding so that the length L and the radius R keep growing even after 3 ns. The width and the length of the jet are much larger than the laser spot size ($250\ \mu\text{m}$), as shown in Table II.

The properties of the jet become more interesting as the ring radius d increases. Figure 4 shows the shape of the jet for different laser ring radii at $t = 3\ \text{ns}$. Figure 5 shows the evolution of electron/ion temperature, electron density, and flow velocity at TCC for different runs in the FLASH simulation. The quantities are calculated by averaging over a $(200\ \mu\text{m})^3$ cubic around TCC ($r = 0, z = 0.25\ \text{cm}$). The peak electron/ion temperature on-axis is higher for a larger ring radius. Compared to the case where $d = 0$, the temperatures for $d = 800\ \mu\text{m}$ or $d = 1200\ \mu\text{m}$ are about one order of magnitude higher. The peak electron density is the highest for $d = 800\ \mu\text{m}$, which is one order of magnitude higher than the $d = 0$ case. The ratio L/R of the jet becomes larger (see Table II) as d gets larger. A large ring radius also reduces the opening angle of the jet. The flow velocity is hardly affected by increasing d . These results are in good agreement with previous 2D cylindrical hydrodynamic simulations by Fu *et al.*¹⁴ using 2D FLASH. The simulations in this work are in 3D cartesian geometry. The full details of the laser configuration are taken into account. In 3D simulations, even though there is the azimuthal asymmetry of the laser intensity on the target as shown in Fig. 1, the jet is still well collimated and has similar hydrodynamical properties to those in the 2D cylindrical case. The azimuthal asymmetry level for electron density can exceed 10%, and the pattern of density distribution in z -slice resembles a “sun flower” as shown in Fig. 7.

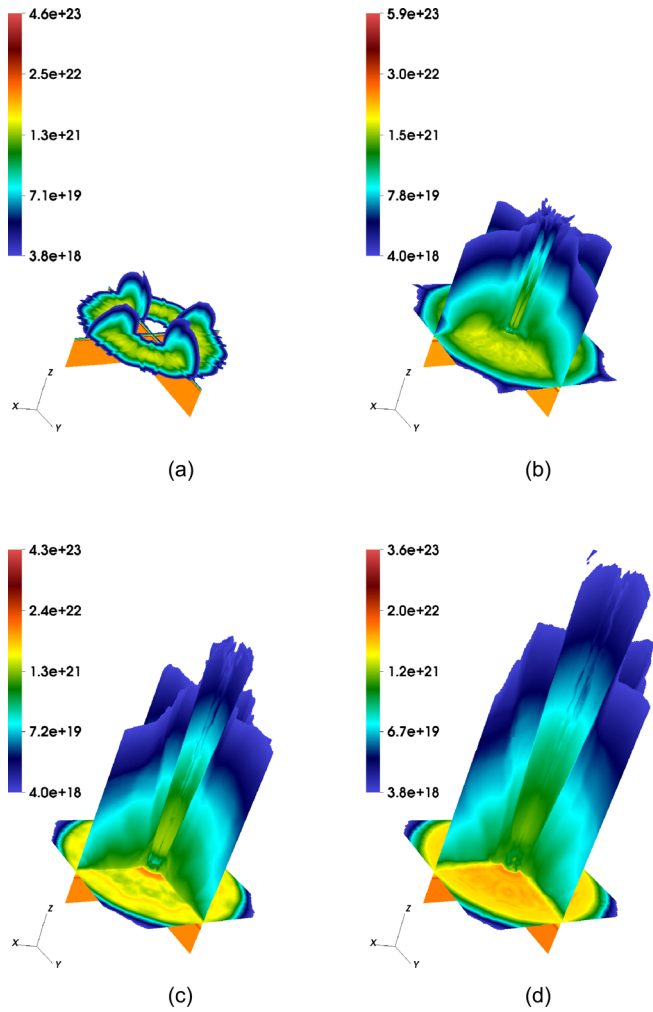


FIG. 3. Three-slice plots for electron density at $x=0$, $y=0$, and $z=0.01$ cm planes in FLASH simulations. The unit is cm^{-3} . The $z=0.01$ cm plane in the simulation is $(0.3\text{ cm})^2$ rectangle. The ring radius is $d=800\ \mu\text{m}$, and the target is CH. (a) $t=0.6$ ns (when laser is still on), (b) $t=1.4$ ns (0.4 ns after the laser is turned off), (c) $t=2.2$ ns, and (d) $t=3.0$ ns. These plots show the time evolution of the jet.

TABLE II. Comparison of plasma properties for different ring radii and targets at $t=3$ ns and $r=0$, and $z=2.5$ mm. n_e , ρ , T_e , T_i , and B are calculated by averaging over a $(200\ \mu\text{m})^3$ cubic around TCC. The jet length L is the defined by the point on the z axis where electron density drops to $3 \times 10^{18}\ \text{cm}^{-3}$. Radius R is defined by reading the position in the $z=2.5$ mm plane where the density scale height $|\nabla \log \rho|^{-1}$ reaches the minimum. Columns 2 to 5 are for pure CH targets. Columns 6 and 7 are for 2% Fe dopant targets.

Plasma property	$d=0$	$d=400\ \mu\text{m}$	$d=800\ \mu\text{m}$	$d=1200\ \mu\text{m}$	$d=800\ \mu\text{m}$ 2% Fe dopant	$d=1200\ \mu\text{m}$ 2% Fe dopant
Electron density n_e (cm^{-3})	1.7×10^{19}	1.2×10^{20}	2.0×10^{20}	1.5×10^{20}	2.7×10^{20}	1.6×10^{20}
Electron temperature T_e (eV)	81	2.1×10^2	5.1×10^2	1.0×10^3	3.9×10^2	8.5×10^2
Ion temperature T_i (eV)	76	2.2×10^2	5.7×10^2	1.4×10^3	5.9×10^2	2.4×10^3
Magnetic field B (gauss)	2.4×10^4	1.4×10^5	3.3×10^5	3.1×10^5	3.5×10^5	3.7×10^5
Jet width R (cm)	>0.15	0.091	0.049	0.039	0.047	0.042
Jet length L (cm)	0.46	0.52	0.54	0.53	0.55	0.50
L/R	<3.1	5.7	11	13.6	11.7	11.9

The jet for the 2% Fe dopant shot is slightly different from the one without the dopant, as shown in Fig. 6. The jet in a dopant shot radiates several times more than that in a non-dopant shot. But the radiative cooling time at $t=3$ ns for the jet is much larger than nanosecond even in the dopant shot. Thus, the radiation cooling (see Table III) has little to do with the shape of the jet after it has grown to millimeter size. For an earlier time, however, the cooling rate is large enough to play a role. As a result, the electron temperature at TCC for doped jets is always lower than that for non-doped jets with the same ring radius d . The reduction in electron temperature relaxes the cylindrical shock. Thus, more electrons flow into the core, which causes the jets in dopant shots to have higher electron density than the non-dopant ones. In both doped and non-doped cases, the jets are always optically thin.

A list of on-axis plasma properties from a snapshot in FLASH simulation results is listed in Table IV using the snapshot for the $d=800\ \mu\text{m}$ case at $t=3$ ns. Other relevant physical terms can be deduced from the scales and dimensionless numbers in Table IV. The plasma in the jet is fully ionized, i.e., $A=6.5$ and $Z=3.5$ for non-doped shots and $A=7.49$ and $Z=3.95$ for doped shots. The optical Thomson scattering diagnostics are simulated and discussed in Sec. IV A. By including laser energy deposition from the probe beam, the hydrodynamical variables in a small region of around $(100\ \mu\text{m})^3$ will change significantly. This effect is significant for the analysis of diagnostics but not of main interest in the dynamical evolution of the jet.

B. Magnetic fields

Without any initial magnetic fields, the seed magnetic field is generated via the Biermann battery term caused by the individual beam heating. The azimuthal asymmetry in the system is significant for the generation of seed fields. In Table IV, the Hall number Ω_H is much larger than the Biermann number Bi . The Hall term is zero if $\mathbf{B}=0$, so it does not generate seed fields. Thus, the Hall term $[-\frac{c}{e} \nabla \times \frac{(\nabla \mathbf{B}) \times \mathbf{B}}{4\pi n_e}]$ is neglectable in our system. The Biermann battery term is the only source term in the generalized Ohm's law that we calculate in FLASH simulation. Magnetic resistivity is also included in the computation. However, due to the large magnetic Reynolds number, magnetic reconnection can hardly happen until later on in the MHD picture.

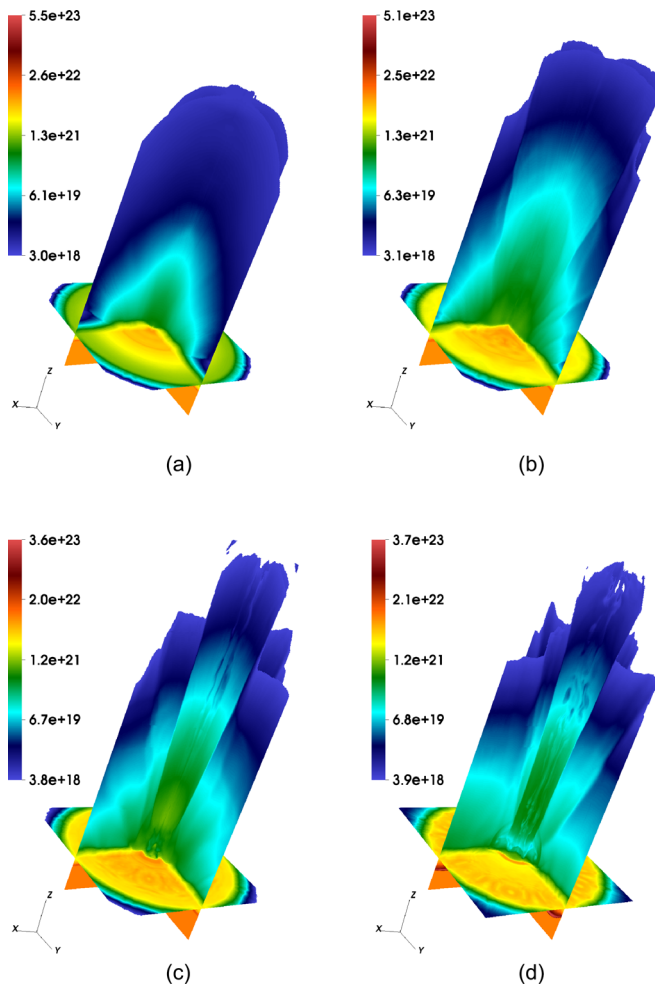


FIG. 4. Three-slice plots for electron density at $x=0$, $y=0$, and $z=0.01$ cm planes at $t=3$ ns for four different ring radii d in FLASH simulations. The unit is cm^{-3} . The scale is the same as in Fig. 3. The targets are CH. (a) $d=0$, (b) $d=400 \mu\text{m}$, (c) $d=800 \mu\text{m}$, and (d) $d=1200 \mu\text{m}$. (c) is the same as Fig. 3(d).

The generation and evolution of the axial dominant magnetic field are demonstrated in Fig. 7. Because of the radial temperature gradient [see Fig. 7(a)] and the azimuthal density gradient [see Fig. 7(b)], the Biermann battery term ($\frac{e}{c} \nabla \times \frac{\nabla P_e}{n_e} = \frac{cB_{\theta}}{e} \nabla T_e \times \nabla n_e$) is mainly in the axial direction. Toroidal dominated magnetic fields are only generated near the surface of the target, where there is a little azimuthal density gradient but a large axial density gradient. At a millimeter above the target surface, the magnetic field is generated in the surrounding [the ring near $r \approx 0.08$ cm in Fig. 7(c)] and advected into the core [the central part of Fig. 7(d)]. The shock amplifies the axial magnetic field by a factor of ~ 4 due to the flux conservation as the plasma flows from the surrounding to the core. The cylindrical shock makes the magnetic field highly concentrated as shown in Fig. 7(e). Because the gradient of density alternates several times azimuthally, the generated axial field also alternates. The 5-fold symmetry in the field comes from the 5-fold symmetry in

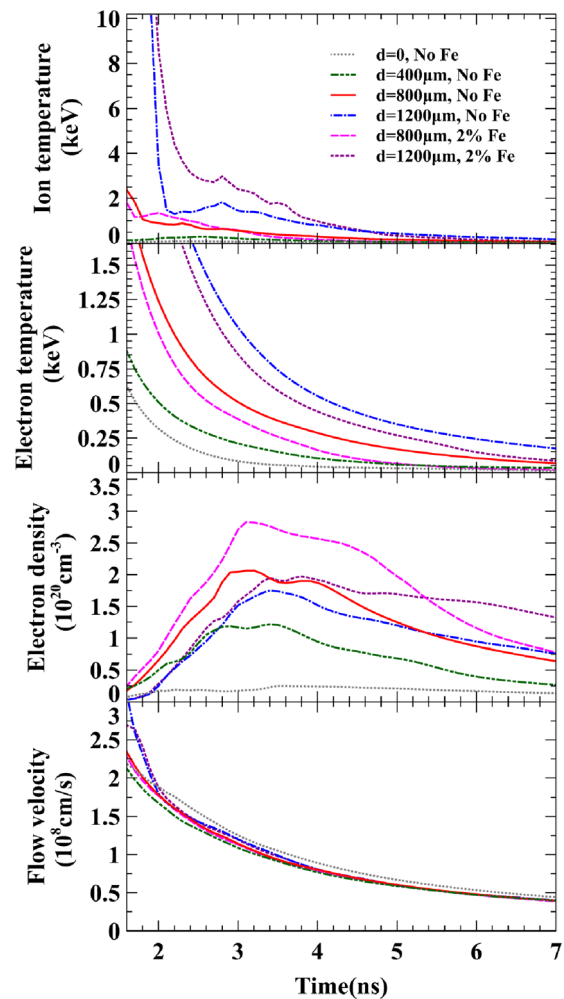


FIG. 5. The evolution of plasma variables at TCC for the six different runs in FLASH simulation. Four sub-figures share the time axis and legends. The quantities are calculated by averaging over a $(200 \mu\text{m})^3$ cubic around TCC.

arranging the laser spots as shown in Fig. 1. The symmetry is slightly broken in the simulation due to the cubic cells and finite resolution. By using a larger ring of laser spots, the magnetic energy is more concentrated in the core of the jet as shown in Figs. 9 and 10.

The magnetic field is mostly axial near the z axis and mostly toroidal near the surface of the target, as shown in Figs. 7(f) and 8. The width and the length of the field bundles grow with the jet. The maximum field strength reaches several hundred kilogauss. The maximum magnitude of the magnetic field at $t=3.6$ ns increases with the radius d of the laser ring, as shown in Fig. 10. This is consistent with the 2D cylindrical simulation.¹⁵ However, the full three dimensional simulation predicts a magnetic field axial polarized and much stronger than that in the two dimensional cylindrical simulation. In the 2D cylindrical simulation, the laser intensity is azimuthally uniform, and thus, the Biermann battery term only has the toroidal component.

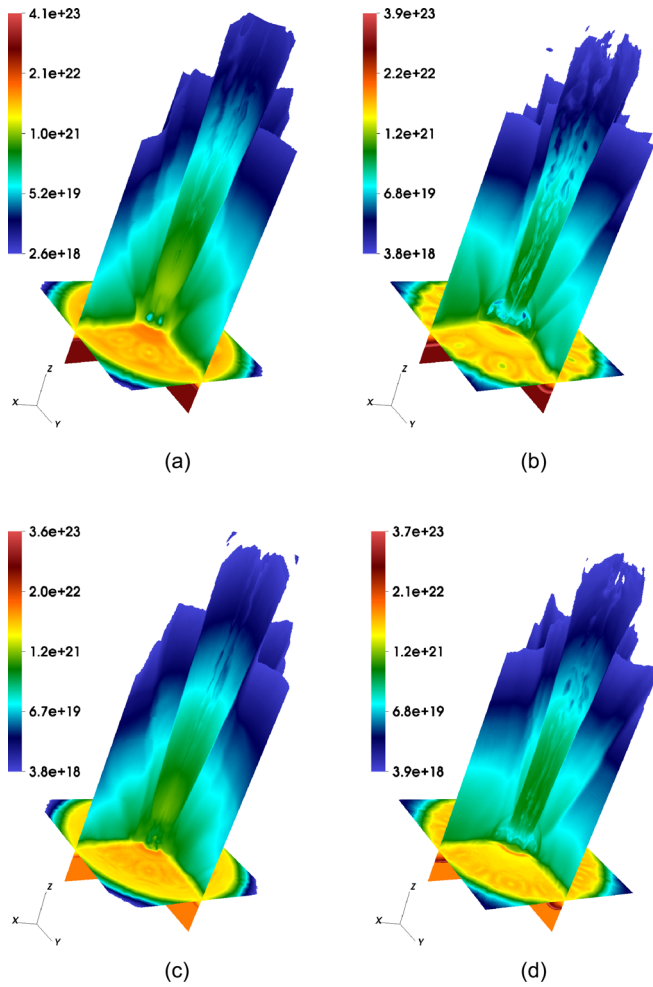


FIG. 6. Three-slice plots for electron density (unit: cm^{-3}) at $x=0$, $y=0$, and $z = 0.01$ cm planes at $t = 3$ ns for two different ring radii d and for two different types of targets in FLASH simulations. The unit is cm^{-3} . The scale is the same as in Fig. 3. (a) $d = 800 \mu\text{m}$, 2% Fe-doped target, (b) $d = 1200 \mu\text{m}$, 2% Fe-doped target, (c) $d = 800 \mu\text{m}$, CH target, and (d) $d = 1200 \mu\text{m}$, CH target. (c) is the same as Fig. 4(c), and (d) is the same as Fig. 4(d).

IV. DIAGNOSTICS MODELING AND COMPARISON TO EXPERIMENTS

A. Optical Thomson scattering spectrum

Although we can fit the optical Thomson-scattering spectrum using the theoretical spectrum to infer the temperatures, density, and flow velocity, the gradient of these quantities near TCC can affect the spectrum and mislead the interpretation. As shown in Table IV, the variation of some quantities can exceed 10% and thus significantly alters the spectrum. Moreover, the 2ω probe beam can potentially heat the plasma near TCC. In our simulation, the heating effect and all the gradients are taken into account. Instead of directly comparing the deduced quantities with those predicted in Fig. 5, we compare the synthetic spectrum with the data for the experimental spectrum in Fig. 11.

TABLE III. Radiation properties of the jet at TCC for $d = 800 \mu\text{m}$ ring radius. The temperature and density are in Table II.

Plasma property	Formula	Value
Planck opacity κ_P (cm^2/g) for CH target	from PROPACEOS	1.8×10^{-2}
Optical depth τ for CH target	$\kappa_P \rho L$	1.1×10^{-6}
Cooling rate (1/s) for CH target	$0.72AZ^{-1} \kappa_P T_e^3$	3.2×10^6
Planck opacity κ_P (cm^2/g) for 2% Fe dopant target	from PROPACEOS	3.9×10^{-1}
Optical depth τ for 2% Fe dopant target	$\kappa_P \rho L$	4.4×10^{-6}
Cooling rate (1/s) for 2% Fe dopant target	$0.72AZ^{-1} \kappa_P T_e^3$	3.2×10^7

Figures 11(a) and 11(b) show that the heating from the TS probe has a significant impact on the measured spectra. Although the energy in the probe beam (25–50 J) is low compared to the drive beams, the $70 \mu\text{m}$ diameter focal spot results in an intensity of $10^{15} \text{W}/\text{cm}^2$. FLASH simulations are performed with and without the probe beam to study the impact of probe-beam heating. The locations of the TS peaks in the simulated spectra that included the probe beam are in much better agreement with the measured spectra. The effect is more pronounced for smaller ring radii because the electron temperature is lower, which leads to higher collisional absorption.

The background of the measured EPW spectrum comes from the bremsstrahlung radiation, which is not calculated in the simulation. The bremsstrahlung shape is apparent when the electron density is larger than $\sim 10^{20} \text{cm}^{-3}$.

The agreement for the IAW spectrum is excellent for $d = 0$ when the heating is included, as shown in the first plot in Fig. 11(b). However, for finite d , the simulation always underestimates the width of the broadened line. The depth of the valley in the middle of the shape is corrected by including the heating effect, which can be explained by the increase in the electron temperature from probe heating. The under-predicted width of the IAW spectrum indicates the under-predicted ion temperature. Because ions are not directly heated by the probe beam, we also compare the ion temperature from fitting the IAW spectrum and the $(200 \mu\text{m})^3$ averaged value in FLASH simulations in Fig. 12.

One may argue that the reason for underestimating the IAW line width is the inaccuracy of the RAGE-like (it is so named because it is identical to the method implemented in the radiation hydrodynamic code RAGE³⁴) energy apportion in our modeling. The RAGE-like approach apportions the work term among the ions, electrons, and radiation field in proportion to the partial pressures of these components. It is physically accurate in smooth flow but does not distribute internal energy correctly among the ions, electrons, and radiation field at shocks. For the finite d case, strong and multiple shocks are presented. There are the shocks between the plumes generated by neighboring beams and the cylindrical shock surrounding the core. The core is usually a secondary downstream. The ion heating exists at all shocks but is not calculated accurately using the RAGE-like approach. The electron temperature should be significantly overestimated if the energy apportion between electrons and ions is inaccurate. However, the comparison between the measured IAW spectrum and the synthetic spectrum with probe heating does not suggest any significant overestimation of

TABLE IV. Simulated plasma properties for case $d = 800 \mu\text{m}$, $t = 3 \text{ ns}$ at $z = 2.5 \text{ mm}$ in non-dopant run. All quantities are in cgs units except temperatures expressed in eV. The length scale is L approximately the width of the jet at $z = 2.5 \text{ mm}$, which is $L \approx 1 \text{ mm}$. n_e , ρ , T_e , and T_i at $r = 0$ are calculated by averaging over a $(200^3 \mu\text{m})^3$ cubic around TCC. n_e , ρ , T_e , and T_i at $r = 1 \text{ mm}$ are calculated by averaging over a $200 \mu\text{m}$ high and $200 \mu\text{m}$ thick ring around $r = 1 \text{ mm}$, $z = 2.5 \text{ mm}$. B is calculated using the root of mean square in the same cubic. The variation of n_e is $\Delta n_e = \sqrt{\overline{n_e^2} - \overline{n_e}^2}$, similar for other variables.

Plasma property	Formula	Value at $r = 0$	Value at $r = 1 \text{ mm}$
Electron density n_e (cm^{-3})	...	2.0×10^{20}	3.0×10^{19}
Δn_e (cm^{-3})	...	1.5×10^{19}	4.1×10^{18}
Mass density ρ (g/cm^3)	...	6.3×10^{-4}	1.1×10^{-4}
$\Delta \rho$ (g/cm^3)	...	4.7×10^{-5}	1.3×10^{-5}
Electron temperature T_e (eV)	...	5.1×10^2	3.9×10^2
ΔT_e (eV)	...	1.2	1.4
Ion temperature T_i (eV)	...	5.7×10^2	1.8×10^2
ΔT_i (eV)	...	1.2×10^2	17
Magnetic field B (gauss)	...	3.3×10^5	4.6×10^4
ΔB (gauss)	...	1.5×10^5	3.0×10^4
Average ionization Z	...	3.5	3.5
Average atomic weight A	...	6.5	6.5
Flow velocity $u \approx u_z$ (cm/s)	...	1.1×10^8	1.1×10^8
Δu (cm/s)	...	3.2×10^6	...
Perpendicular velocity $\sqrt{u_x^2 + u_y^2}$ (cm/s)	...	2.7×10^6	1.5×10^7
Sound speed c_s (cm/s)	$9.8 \times 10^5 \frac{[ZT_{\text{elec}} + 1.67T_{\text{ion}}]^{1/2}}{A^{1/2}}$	2.0×10^7	1.6×10^7
Mach number M	u/c_s	5.5	6.8
Electron plasma frequency (rad/s)	$5.6 \times 10^4 n_e^{1/2}$	7.9×10^{14}	3.1×10^{14}
Coulomb logarithm $\ln \Lambda$	$23.5 - \ln(n_e^{1/2} T_e^{-5/4}) - [10^{-5} + (\ln T_e - 2)^2 / 16]^{1/2}$	6.9	7.5
Electron thermal velocity v_{Te} (cm/s)	$4.2 \times 10^7 T_e^{1/2}$	9.5×10^8	8.3×10^8
Electron collision rate ν_e (1/s)	$2.9 \times 10^{-6} n_e \ln \Lambda T_e^{-3/2}$	3.5×10^{11}	8.5×10^{10}
Electron-ion collision rate ν_{ei} (1/s)	$3.2 \times 10^{-9} Z A^{-1} n_e \ln \Lambda T_e^{-3/2}$	2.1×10^8	5.1×10^7
Electron mean free path l_e (cm)	v_{Te} / ν_e	2.7×10^{-3}	9.8×10^{-3}
Electron gyro-frequency ω_{ce} (rad/s)	$1.7 \times 10^7 B$	5.6×10^{12}	7.8×10^{11}
Electron gyroradius r_e (cm)	$2.4 T_e^{1/2} B^{-1}$	1.6×10^{-4}	7.0×10^{-4}
Ion thermal velocity v_{Ti} (cm/s)	$9.8 \times 10^5 A^{-1/2} T_i^{1/2}$	9.2×10^6	2.9×10^6
Ion collision rate ν_i (1/s)	$4.8 \times 10^{-8} Z^3 n_e A^{-1/2} \ln \Lambda T_i^{-3/2}$	8.2×10^{10}	1.8×10^{14}
Ion mean free path l_i (cm)	v_{Ti} / ν_i	1.1×10^{-4}	1.6×10^{-8}
Ion gyro-frequency ω_{ci} (rad/s)	$9.6 \times 10^3 Z B / A$	1.7×10^9	2.4×10^8
Ion gyroradius r_i (cm)	$1.0 \times 10^2 A^{1/2} Z^{-1} T_i^{1/2} B^{-1}$	5.3×10^{-3}	2.1×10^{-2}
Plasma β	$\frac{2.4 \times 10^{-12} n_e (T_e + T_i / Z)}{B^2 / (8\pi)}$	75	3.8×10^2
Kinetic energy/thermal energy	$\frac{\frac{1}{2} m_p n_e A u^2}{2.4 \times 10^{-12} n_e (T_e + T_i / Z)}$	12	18
Reynolds number Rm	$uL / \nu \left(\eta = 1.9 \times 10^{19} \frac{T_i^{5/2}}{A^{1/2} Z^3 n_e \ln \Lambda} \right)$	1.1×10^4	3.3×10^4
Magnetic Reynolds number Re	$uL / \eta \left(\eta = 3.2 \times 10^5 \frac{Z \ln \Lambda}{T_e^{3/2}} \right)$	1.6×10^4	1.0×10^4
Biermann number Bi	$\frac{euBL}{ck_B T_e}$	71	13
Hall number Ω_H	$\frac{4\pi en_e uL}{Bc}$	1.3×10^3	1.4×10^3

electron temperature. The reason for this might be the usage of electron heat conduction in FLASH simulation, which mitigates the inaccuracy of energy apportion. The extra part of the ion thermal energy measured by the IAW spectrum can only come from part of the kinetic energy in the axial bulk motion of the

flow, since multiple shocks already convert the kinetic energy of radial and toroidal bulk motion into thermal energy, and the magnetic energy is little compared to the thermal energy and the kinetic energy. For example, 10% of the bulk kinetic energy density at $t = 3 \text{ ns}$ and $z = 2.5 \text{ mm}$ corresponds to

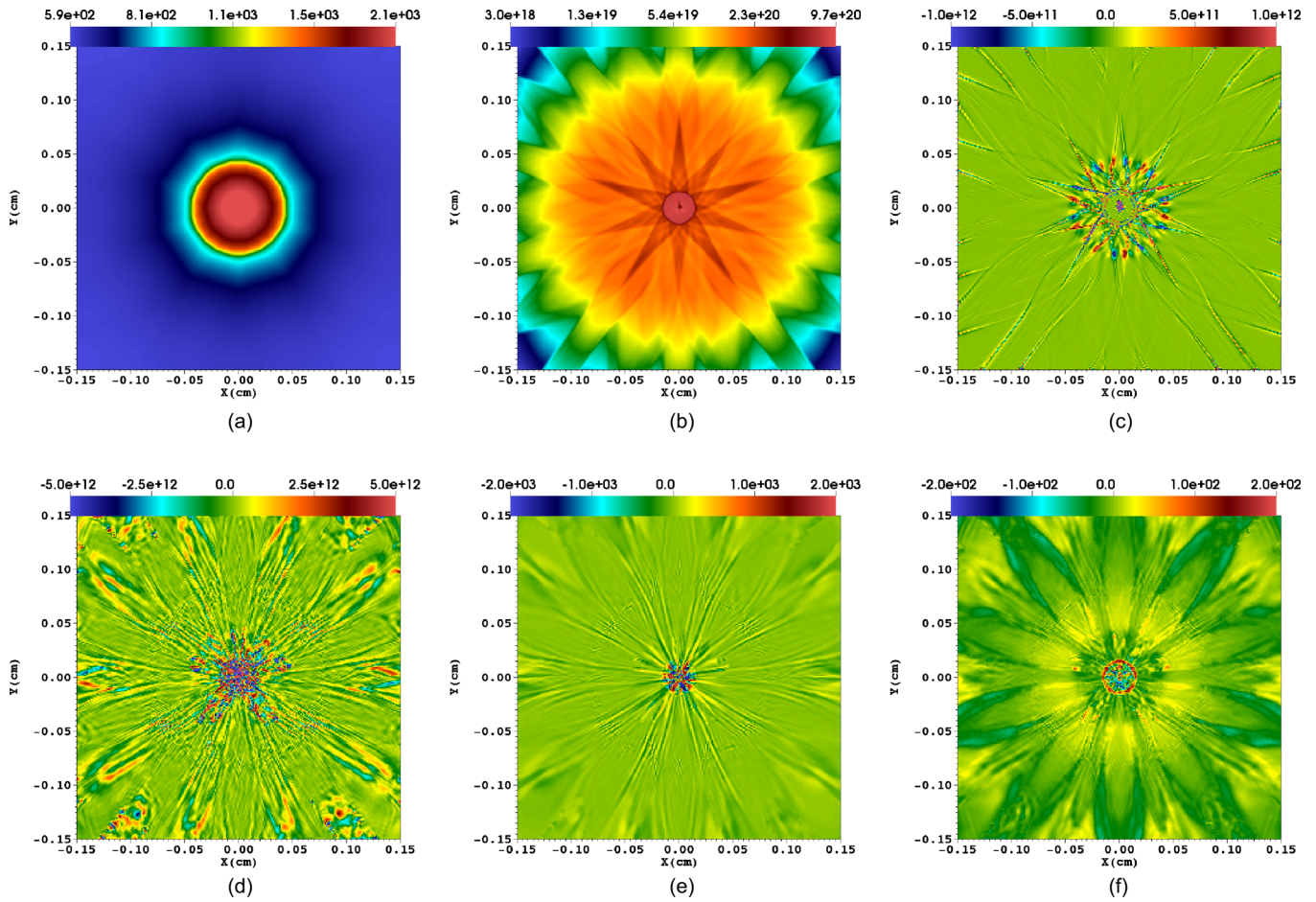


FIG. 7. Slice plot of several quantities at $z = 0.1$ cm for $t = 1.6$ ns. These figures demonstrate the generation and evolution of the axial dominant magnetic field with alternating polarity and 5-fold symmetry (a) Electron temperature (eV). The pattern is concentric circles. (b) Electron density (cm^{-3}). The “sunflower-like” pattern has 5-fold symmetry due to the laser pattern. The symmetry is slightly broken due to the finite number of cells in the simulation (c) z component of the Biermann battery term $\frac{c}{4\pi} \nabla \times \frac{\nabla P_e}{n_e} = \frac{ck_B}{e} \nabla T_e \times \nabla n_e$ (kG/s), (d) z component of the advection term $\nabla \times (\mathbf{v} \times \mathbf{B})$ (kG/s), (e) z component of the magnetic field (kG), and (f) φ component of the magnetic field (kG).

$k_B T_i = 0.1 \times \frac{m_i u^2}{2} \approx 2$ keV. It is likely that the turbulence is developed from the flow velocity difference between the plumes generated from different laser spots due to the laser intensity difference between these spots. The plasma has a high Reynolds number, as shown in Table IV. The kinetic energy in turbulent motion does not have to be dissipated into heat to make the IAW spectrum broader, as long as a significant amount of turbulent kinetic energy is cascaded down to a scale below the resolution of Thomson scattering, i.e., $\sim 100 \mu\text{m}$. We will study the turbulence effect in a future work.

B. Proton radiography

The proton images are smeared by a few factors (1) Spatial smearing: the finite size of the proton source, which is $\sim 45 \mu\text{m}$ for the fusion protons and $\sim 5 \mu\text{m}$ for the TNSA protons; (2) Temporal smearing: the pulse duration of the proton source, which is ~ 150 ps for fusion protons and 1 ps for TNSA protons. The pulse duration Δt causes the smearing at the length scale

$\Delta l \sim v \Delta t$, where v is the characteristic speed of the plasma. For fusion protons, $\Delta l_z \sim 160 \mu\text{m}$, $\Delta l_{x,y} \sim 13 \mu\text{m}$, using the velocities in Table IV. For TNSA protons with $E = 10$ MeV, $\Delta l_z \sim 1 \mu\text{m}$, $\Delta l_{x,y} \sim 0.15 \mu\text{m}$; (3) Spectrum smearing: the energy variation ΔE of the source proton. Derived from Eq. (16) in the study by Graziani *et al.*,³⁵ the variation of the deflection angle caused by ΔE is $\frac{\Delta E}{E}$ times the deflection angle. If there is only spectrum smearing, assuming that the proton is shifted by $200 \mu\text{m}$ (which is typical) seen in the TCC frame, it is expected that the 10.2 MeV TNSA protons with $\frac{\Delta E}{2E} = \frac{3.79 \text{ MeV}/2}{2 \times 10.2 \text{ MeV}}$ (ΔE is half of the effective temperature) resolve the magnetic field at $\sim 20 \mu\text{m}$, DD protons with $\frac{\Delta E}{2E} = \frac{0.32 \text{ MeV}}{2 \times 3 \text{ MeV}}$ resolve the magnetic field at $\sim 11 \mu\text{m}$, and D^3He protons with $\frac{\Delta E}{2E} = \frac{0.67 \text{ MeV}}{2 \times 14.7 \text{ MeV}}$ resolve the magnetic field at $\sim 5 \mu\text{m}$. The energy gain or lost from the electric field is estimated to be less than 0.1 MeV, which is negligible compare to ΔE of the beam itself. Overall, our FLASH simulation is able to resolve a smaller spatial scale than the experiment.

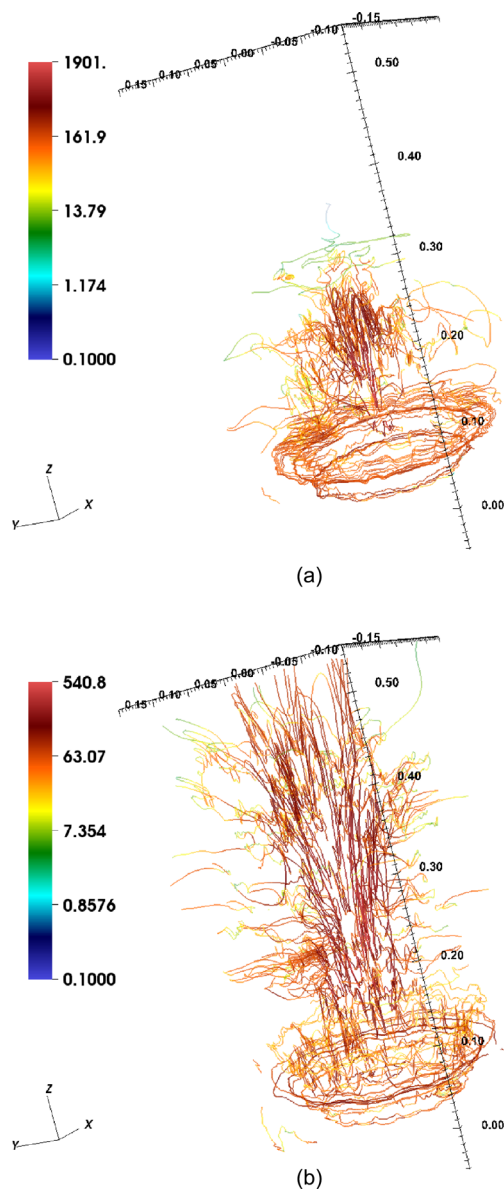


FIG. 8. Sample magnetic field lines (color scale unit: kG) for $d = 800$ cm, CH target. (a) at $t = 1.6$ ns (b) at $t = 3.6$ ns. The field far away from the target is mainly axial and the field close to the target is toroidal.

The simulation of images predicts the features observed in the experimental data. To the lowest order, the light and dark patterns correspond to the averaged MHD current ($\nabla \times \mathbf{B}$) projected along the light of sight.³⁵ The alternating axial field filaments result in several vertical dark and bright strips. The curved horizontal strip close to the surface of the target is produced by the large loop of the surface toroidal field. Figure 13 shows the comparison between the simulation synthetic and experimental D^3He proton images. Figure 14 shows the comparison between the simulation synthetic and experimental

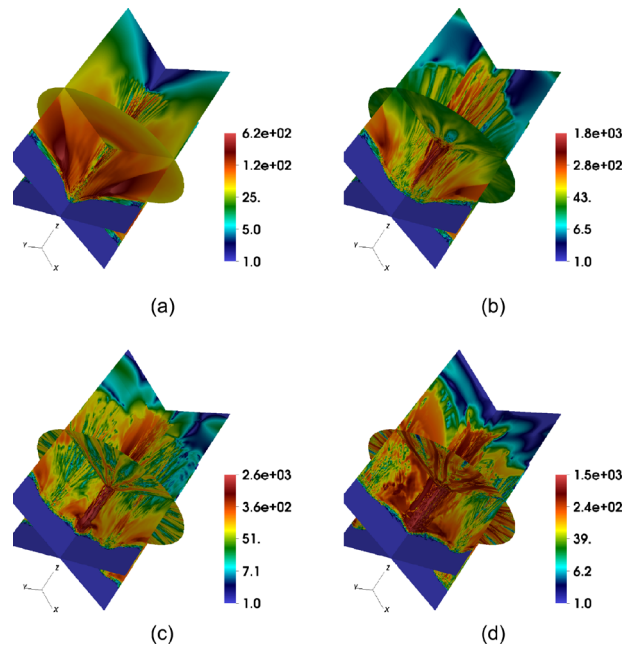


FIG. 9. Three slice plot for magnetic field amplitude (unit:kG) at $x=0, y=0,$ and $z = 0.1$ cm for different laser ring radii d at $t = 1.6$ ns. The disk slice is at $z = 0.1$ cm with a diameter of 0.3 mm. (a) $d = 0,$ (b) $d = 400 \mu\text{m},$ (c) $d = 800 \mu\text{m},$ and (d) $d = 1200 \mu\text{m}.$

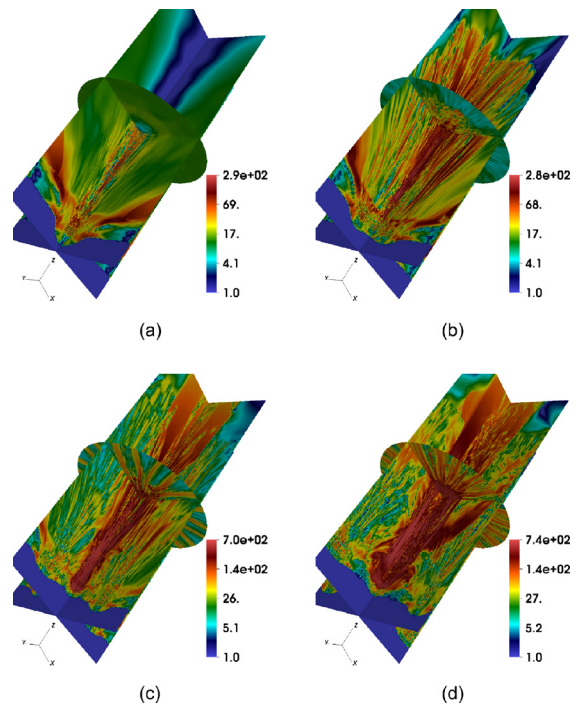


FIG. 10. Three slice plot for magnetic field amplitude (unit:kG) at $x=0, y=0,$ and $z = 0.25$ cm for different laser ring radii d at $t = 3.6$ ns. The disk slice is at $z = 0.25$ cm with a diameter of 0.3 mm. (a) $d = 0,$ (b) $d = 400 \mu\text{m},$ (c) $d = 800 \mu\text{m},$ and (d) $d = 1200 \mu\text{m}.$

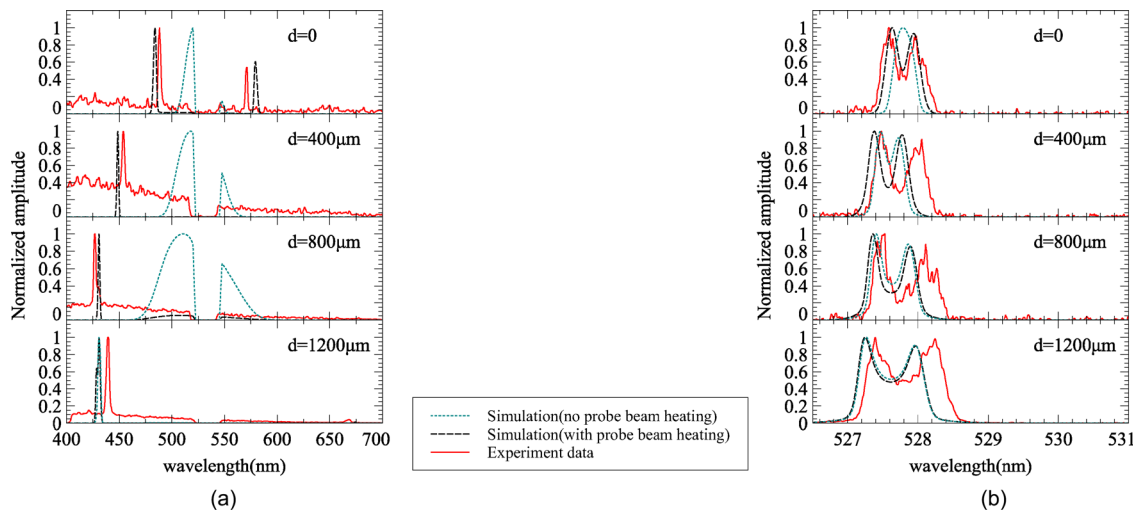


FIG. 11. Comparison between the synthetic optical Thomson-scattering spectra based on FLASH simulations and the experimental data. The red solid line is the experimental data, the blue dotted line is the synthetic spectrum without probe beam heating, and the black dashed line is the synthetic spectrum with probe beam heating. (a) EPW spectrum at 3.6 ns. (b) IAW spectrum at 3.9 ns.

10.2 MeV TNSA proton images. Figure 15 shows examples of the proton images for $d = 400 \mu\text{m}$ and $d = 1200 \mu\text{m}$ cases. Good qualitative agreement between the synthetic images and the ones from experiment on the general trend of large scale features suggests that the magnetic field structures we predict using FLASH simulation are consistent with the structures in the experiments.

The Nernst effect can affect the evolution of the magnetic field.^{36,37} This might be the reason why there are some disagreements in small scale structures and sizes between the experimental data and the synthetic images. In Table IV, the product of the electron gyro-frequency ω_{ce} and electron collision time $\tau_e (=1/\nu_e)$ is $\omega_{ce}\tau_e \sim 15$ at $r=0$ and $\omega_{ce}\tau_e \sim 9$ at $r=1\text{mm}$. The value $\omega_{ce}\tau_e > 1$ indicates that the Nernst effect is important for our experiments. The MHD model with the Nernst term will be implemented in FLASH in the future. We will make detailed qualitative comparison in a future study with the Nernst term included.

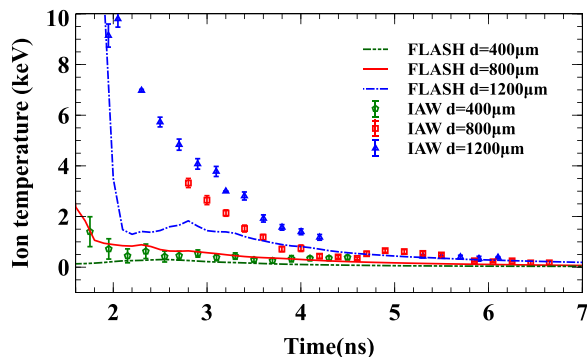


FIG. 12. The data for ion temperature from fitting the IAW spectrum and the $(200 \mu\text{m})^3$ averaged value in FLASH simulations, both at TCC.

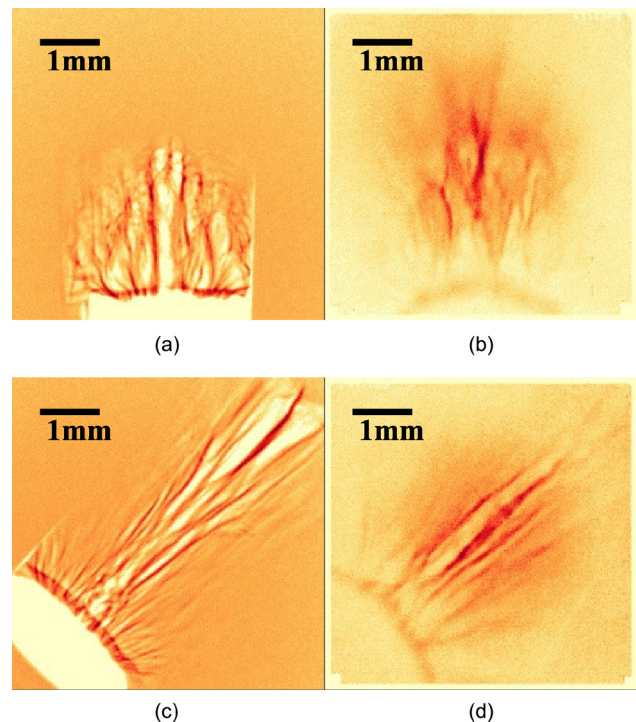


FIG. 13. Comparison of the synthetic proton image with data recorded on CR39 for 14.7 MeV protons. The color scales are the same for all images. The ring radius is $d = 800 \mu\text{m}$. The target is CH without the dopant. (a) The synthetic image at $t = 1.6 \text{ ns}$, and the corresponding three-slice plot of the field is in Fig. 9(c). (b) The experimental image at $t = 1.6 \text{ ns}$, (c) synthetic image at $t = 3.6 \text{ ns}$, and the corresponding three-slice plot of the field is in Fig. 10(c). (d) The experimental image at $t = 3.6 \text{ ns}$. The CR39 image plate is $10 \text{ cm} \times 10 \text{ cm}$. On the plot, magnification is taken into account, and the scale listed is in the plasma frame. In (a) and (b), upward is the $+z$ direction. In (c) and (d), upright is the $+z$ direction. The void region in below in (a) and (b), and bottom left corner in (c) and (d) is the target, which block the protons.

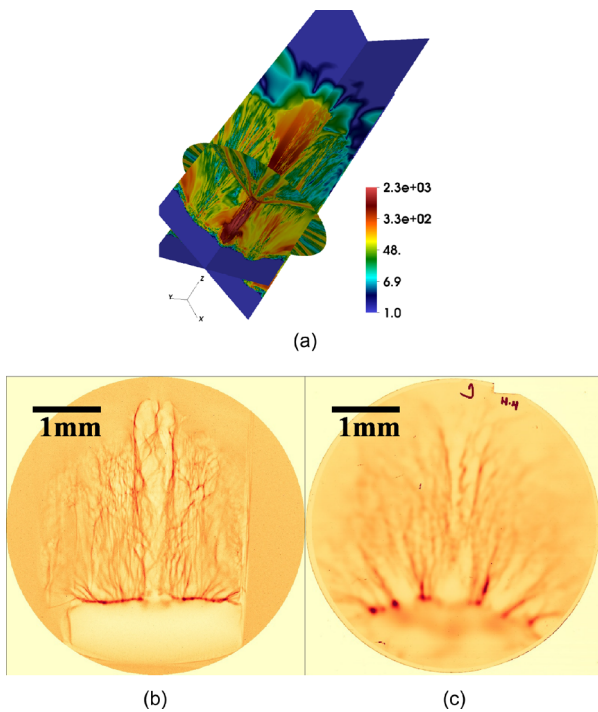


FIG. 14. Comparison of the synthetic proton image with data recorded on the radiochromic film for 10.2MeV protons. The color scales are the same for two images. The ring radius is $d = 800 \mu\text{m}$. The target is CH without dopant. (a) three-slice plot at $x=0$, $y=0$, $z = 0.1 \text{ cm}$, magnetic field strength (kG) plot at $t = 1.9 \text{ ns}$, (b) synthetic image at $t = 1.9 \text{ ns}$, and (c) experimental image at $t = 1.9 \text{ ns}$ from H4 pack. The image plate is a disk of 10 cm. The scale and orientation are the same as in Figs. 13(a) and 13(b).

V. CONCLUSIONS AND DISCUSSIONS

The FLASH simulation results were validated against a subset of experimental data from the OMEGA experiments. The creation of the jets and strong magnetic fields using the ring laser pattern is explained. 3D simulations reproduce some features in previous 2D cylindrical results.^{14,15} However, many new features emerge in 3D, e.g., the “sun flower” density pattern and the alternating para-axial magnetic field bundles. Some questions still remain, e.g., the under-prediction in the line width of the IAW spectrum in Fig. 11. An accurate modeling for the magnetic fields requires implementation of the Nernst effect in the FLASH code. Simulations using higher resolutions are also desired. The XRFC modeling will be discussed in a future study.

The geometry of magnetic fields in our jets may be different from the generally believed models in many astrophysical context, e.g., the magnetic field of the jet along the axis of an accreting black hole,³⁸ where the toroidal field supposedly dominates. However, much can still be learned about the magnetic effect on jet collimation, stability, and structure in the laboratory. The characteristics of the magnetized jet can be well controlled by tuning the ring radius and increasing number of beams. By varying the hollow ring radius, laser, and target properties, we can achieve a large dynamic range for the jet parameters, thus creating a highly versatile laboratory platform for laser-based astrophysics. By using the jets we created, shocks and shear flows can be studied with jet-jet collisions.

The hollow ring laser platform is also ideally suited to scale up to NIF with 192 beams and more energy per beam, creating centimeter-sized magnetized jets. The jets produced with the

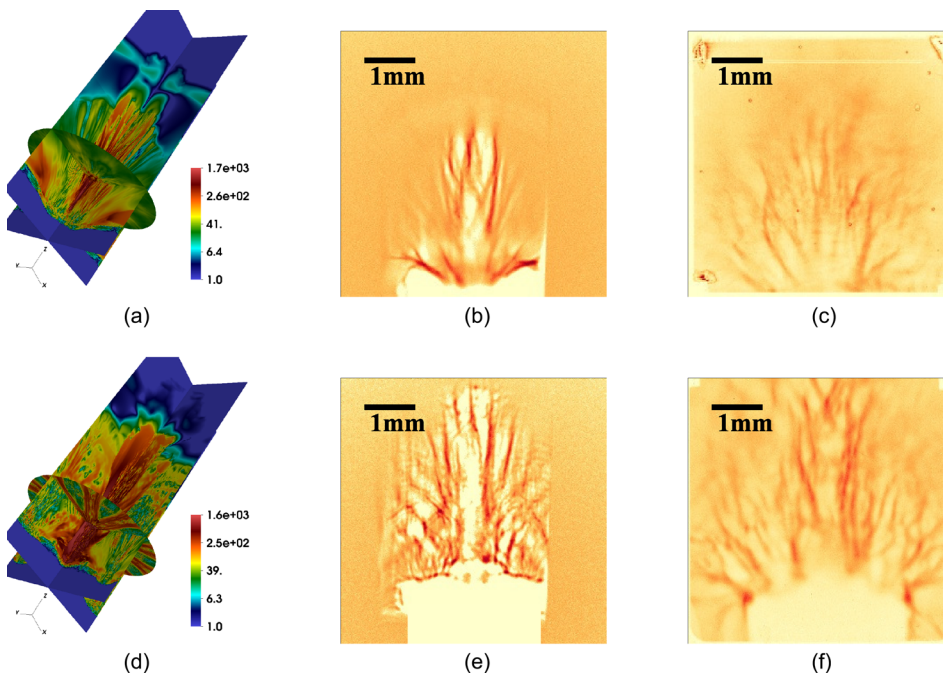


FIG. 15. (a) Three-slice plot at $x=0$, $y=0$, and $z = 0.1 \text{ cm}$ and the magnetic field strength (kG) plot at $t = 1.8 \text{ ns}$ for $d = 400 \mu\text{m}$. (b) The synthetic 3MeV proton image at $t = 1.8 \text{ ns}$ for $d = 400 \mu\text{m}$. (c) The experimental 3MeV proton image at $t = 1.9 \text{ ns}$ for $d = 400 \mu\text{m}$. (d) Three-slice plot at $x=0$, $y=0$, and $z = 0.1 \text{ cm}$ and magnetic field strength (kG) plot at $t = 2.3 \text{ ns}$ for $d = 120 \mu\text{m}$. (e) The synthetic 14.7MeV proton image at $t = 2.3 \text{ ns}$ for $d = 1200 \mu\text{m}$. (f) The experimental 14.7MeV proton image at $t = 2.3 \text{ ns}$ for $d = 1200 \mu\text{m}$. The scale and orientation of the image are the same as in Figs. 13(a) and 13(b). The color scales are the same for all images.

NIF platform will have several distinctive properties from OMEGA experiments but are of key importance for astrophysical jet modeling. The higher temperature, density, flow velocity, and magnetic field will lead to large dimensionless parameters. A turbulence regime is possible. The longer pulse on NIF can sustain the jet for longer time, so that the radiative cooling for doped targets becomes significant and useful to make the aspect ratio larger. The aspect ratio can become large enough ($\gg 10$) that the stability study can become more relevant to astrophysics. The physical parameters of the jet can be tuned in such ways that various collisionless and collisional regimes of the plasma can be accessed. The dimensionless parameters for astrophysical jets may be better realized in the large scale jets of NIF. Magnetic field geometry may be tuned by increasing the number of beams.

ACKNOWLEDGMENTS

This research was supported by DOE Grant DE-NA0002721. The research and materials incorporated in this work were partially developed at the National Laser Users' Facility at the University of Rochester's Laboratory for Laser Energetics (LLE), with the financial support from the U.S. Department of Energy (DOE) under Cooperative Agreement DE-NA0001944. This work used the Extreme Science and Engineering Discovery Environment (XSEDE³⁹) which was supported by the National Science Foundation (NSF) Grant No. ACI-1548562. This research used resources of the National Energy Research Scientific Computing Center, a DOE Office of Science User Facility supported by the Office of Science of the U.S. Department of Energy under Contract No. DE-AC02-05CH11231. Additional simulations were performed at the Argonne Leadership Computing Facility and with Los Alamos National Laboratory institutional computing. Y.L. and E.L. acknowledge partial support by LANL-LDRD during the writing of this paper. We also acknowledge the valuable discussions with Hui Li.

REFERENCES

- ¹S. Hirose, Y. Uchida, K. Shibata, and R. Matsumoto, *Publ. Astron. Soc. Jpn.* **49**, 193 (1997).
- ²A. Ferrari, *Annu. Rev. Astron. Astrophys.* **36**, 539 (1998).
- ³R. Sari, T. Piran, and J. P. Halpern, *Astrophys. J.* **519**, L17 (1999).
- ⁴P. Tzeferacos, A. Rigby, A. Bott, A. R. Bell, R. Bingham, A. Casner, F. Cattaneo, E. M. Churazov, J. Emig, N. Flocke, F. Fiuza, C. B. Forest, J. Foster, C. Graziani, J. Katz, M. Koenig, C.-K. Li, J. Meinecke, R. Petrasso, H.-S. Park, B. A. Remington, J. S. Ross, D. Ryu, D. Ryutov, K. Weide, T. G. White, B. Reville, F. Miniati, A. A. Schekochihin, D. H. Froula, G. Gregori, and D. Q. Lamb, *Phys. Plasmas* **24**, 041404 (2017).
- ⁵P. Tzeferacos, A. Rigby, A. F. A. Bott, A. R. Bell, R. Bingham, A. Casner, F. Cattaneo, E. M. Churazov, J. Emig, F. Fiuza, C. B. Forest, J. Foster, C. Graziani, J. Katz, M. Koenig, C.-K. Li, J. Meinecke, R. Petrasso, H.-S. Park, B. A. Remington, J. S. Ross, D. Ryu, D. Ryutov, T. G. White, B. Reville, F. Miniati, A. A. Schekochihin, D. Q. Lamb, D. H. Froula, and G. Gregori, *Nat. Commun.* **9**, 591 (2018).
- ⁶B. A. Remington, *Plasma Phys. Controlled Fusion* **47**, A191 (2005).
- ⁷J. M. Foster, B. H. Wilde, P. A. Rosen, R. J. R. Williams, B. E. Blue, R. F. Coker, R. P. Drake, A. Frank, P. A. Keiter, A. M. Khokhlov, J. P. Knauer, and T. S. Perry, *Astrophys. J.* **634**, L77 (2005).
- ⁸A. Ciardi, S. V. Lebedev, A. Frank, E. G. Blackman, J. P. Chittenden, C. J. Jennings, D. J. Ampleford, S. N. Bland, S. C. Bott, J. Rapley, G. N. Hall, F. A. Suzuki-Vidal, A. Marocchino, T. Lery, and C. Stehle, *Phys. Plasmas* **14**, 056501 (2007).
- ⁹A. Ciardi, S. V. Lebedev, A. Frank, F. Suzuki-Vidal, G. N. Hall, S. N. Bland, A. Harvey-Thompson, E. G. Blackman, and M. Camenzind, *Astrophys. J.* **691**, L147 (2009).
- ¹⁰S. V. Lebedev, D. Ampleford, A. Ciardi, S. N. Bland, J. P. Chittenden, M. G. Haines, A. Frank, E. G. Blackman, and A. Cunningham, *Astrophys. J.* **616**, 988 (2004).
- ¹¹S. V. Lebedev, A. Ciardi, D. J. Ampleford, S. N. Bland, S. C. Bott, J. P. Chittenden, G. N. Hall, J. Rapley, C. Jennings, M. Sherlock, A. Frank, and E. G. Blackman, *Plasma Phys. Controlled Fusion* **47**, B465 (2005).
- ¹²S. V. Lebedev, J. P. Chittenden, F. N. Beg, S. N. Bland, A. Ciardi, D. Ampleford, S. Hughes, M. G. Haines, A. Frank, E. G. Blackman, and T. Gardiner, *Astrophys. J.* **564**, 113 (2002).
- ¹³B. A. Remington, R. P. Drake, and D. D. Ryutov, *Rev. Mod. Phys.* **78**, 755 (2006).
- ¹⁴W. Fu, E. P. Liang, M. Fatenejad, D. Q. Lamb, M. Grosskopf, H.-S. Park, B. Remington, and A. Spitkovsky, *High Energy Density Phys.* **9**, 336 (2013).
- ¹⁵W. Fu, E. P. Liang, P. Tzeferacos, and D. Q. Lamb, *High Energy Density Phys.* **17**, 42 (2015).
- ¹⁶L. Biermann, *Z. Naturforsch.*, **A 5**, 65 (1950); available at <http://adsabs.harvard.edu/abs/1950ZNatA...5...65>.
- ¹⁷T. Boehly, D. Brown, R. Craxton, R. Keck, J. Knauer, J. Kelly, T. Kessler, S. Kumpan, S. Loucks, S. Letzring, F. Marshall, R. McCrory, S. Morse, W. Seka, J. Soures, and C. Verdon, *Opt. Commun.* **133**, 495 (1997).
- ¹⁸L. Gao et al., "Mega-gauss plasma jet creation using a ring of laser beams" (unpublished).
- ¹⁹B. Fryxell, K. Olson, P. Ricker, F. X. Timmes, M. Zingale, D. Q. Lamb, P. MacNeice, R. Rosner, J. W. Truran, and H. Tufo, *Astrophys. J. Suppl. Ser.* **131**, 273 (2000).
- ²⁰See <https://flash.uchicago.edu/> for FLASH4.
- ²¹A. Dubey, K. Antypas, M. K. Ganapathy, L. B. Reid, K. Riley, D. Sheeler, A. Siegel, and K. Weide, *Parallel Comput.* **35**, 512 (2009).
- ²²C. Graziani, P. Tzeferacos, D. Lee, D. Q. Lamb, K. Weide, M. Fatenejad, and J. Miller, *Astrophys. J.* **802**, 43 (2015).
- ²³See <http://www.prism-cs.com> for PROPACEOS.
- ²⁴S. I. Braginskii, *Rev. Plasma Phys.* **1**, 205 (1965); available at <http://adsabs.harvard.edu/abs/1965RvPP...1..205B>.
- ²⁵D. H. Froula, J. S. Ross, L. Divol, and S. H. Glenzer, *Rev. Sci. Instrum.* **77**, 10E522 (2006).
- ²⁶D. Froula, P. Davis, L. Divol, J. Ross, N. Meezan, D. Price, S. Glenzer, and C. Rousseaux, *Phys. Rev. Lett.* **95**, 195005–195009 (2005).
- ²⁷J. Sheffield, D. Froula, S. H. Glenzer, and J. N. C. Luhmann, *Plasma Scattering of Electromagnetic Radiation: Theory and Measurement Techniques* (Academic Press, 2010).
- ²⁸R. K. Follett, J. A. Delettrez, D. H. Edgell, R. J. Henchen, J. Katz, J. F. Myatt, and D. H. Froula, *Rev. Sci. Instrum.* **87**, 11E401 (2016).
- ²⁹C. K. Li, F. H. Séguin, J. A. Frenje, J. R. Rygg, R. D. Petrasso, R. P. J. Town, P. A. Amendt, S. P. Hatchett, O. L. Landen, A. J. Mackinnon, P. K. Patel, V. A. Smalyuk, T. C. Sangster, and J. P. Knauer, *Phys. Rev. Lett.* **97**, 135003 (2006).
- ³⁰M. J.-E. Manuel, A. B. Zylstra, H. G. Rinderknecht, D. T. Casey, M. J. Rosenber, N. Sinenian, C. K. Li, J. A. Frenje, F. H. Séguin, and R. D. Petrasso, *Rev. Sci. Instrum.* **83**, 063506 (2012).
- ³¹A. B. Zylstra, C. K. Li, H. G. Rinderknecht, F. H. Séguin, R. D. Petrasso, C. Stoeckl, D. D. Meyerhofer, P. Nilson, T. C. Sangster, S. L. Pape, A. Mackinnon, and P. Patel, *Rev. Sci. Instrum.* **83**, 013511 (2012).
- ³²K. Flippo, T. Bartal, F. Beg, S. Chawla, J. Cobble, S. Gaillard, D. Hey, A. MacKinnon, A. MacPhee, P. Nilson, D. Offermann, S. L. Pape, and M. J. Schmitt, *J. Phys.: Conf. Ser.* **244**, 022033 (2010).
- ³³See <https://physics.nist.gov/PhysRefData/Star/Text/PSTAR.html> for The PSTAR Table.
- ³⁴M. Gittings, R. Weaver, M. Clover, T. Betlach, N. Byrne, R. Coker, E. Dendy, R. Hueckstaedt, K. New, W. R. Oakes, D. Ranta, and R. Stefan, *Comput. Sci. Discovery* **1**, 015005 (2008).

- ³⁵C. Graziani, P. Tzeferacos, D. Q. Lamb, and C. Li, *Rev. Sci. Instrum.* **88**, 123507 (2017).
- ³⁶L. Gao, P. Nilson, I. Igumenshchev, M. Haines, D. Froula, R. Betti, and D. Meyerhofer, *Phys. Rev. Lett.* **114**, 215003 (2015).
- ³⁷L. Lancia, B. Albertazzi, C. Boniface, A. Grisollet, R. Riquier, F. Chaland, K.-C. L. Thanh, P. Mellor, P. Antici, S. Buffechoux, S. Chen, D. Doria, M. Nakatsutsumi, C. Peth, M. Swantusch, M. Stardubtsev, L. Palumbo, M. Borghesi, O. Willi, H. Pépin, and J. Fuchs, *Phys. Rev. Lett.* **113**, 235001 (2014).
- ³⁸K. Beckwith, J. F. Hawley, and J. H. Krolik, *Astrophys. J.* **678**, 1180 (2008).
- ³⁹J. Towns, T. Cockerill, M. Dahan, I. Foster, K. Gaither, A. Grimshaw, V. Hazlewood, S. Lathrop, D. Lifka, G. D. Peterson, R. Roskies, J. R. Scott, and N. Wilkens-Diehr, *Comput. Sci. Eng.* **16**, 62 (2014).